Phase transformations and plasticity in single-crystal iron from shock compression to spall fracture

Nourou Amadou, Thibaut de Rességuier

Phase transformations and plasticity in single-crystal iron from shock compression to spall fracture

N. Amadou[1, 2], T. de Rességuier[1]

[1]Institut Prime, CNRS, ISAE-ENSMA, Université de Poitiers, Poitiers, France

[2] Département de Physique, Université Abdou Moumouni de Niamey, BP. 10662, Niamey, Niger

This is an author version of Phys. Rev. B 108, 174109, 2023, DOI: 10.1103/PhysRevB.108.174109

Non Equilibrium Molecular Dynamics simulations have been used to investigate phase transformations and plasticity in single crystal iron from shock compression to dynamic tension and subsequent spall fracture. In consistence with experimental observations, the unloading wave following the compression front is found to evolve into a rarefaction shock at the reverse hcp to bcc phase transformation, and a pressure hysteresis between the direct and reverse phase transformations is evidenced. The interaction of this unloading wave with the rarefaction wave reflected from the sample free surface classically induces tension within the crystal, which is found to drive a bcc to fcc phase transformation in agreement with very recent experimental observation under subnanosecond laser shock loading. At the atomic scale, the mechanism governing this bcc to fcc phase transformation is consistent with a Bain transformation path. The spall fracture process is observed to occur through voids nucleation and growth either at favorable sites (twin boundaries, bcc-fcc grain boundaries after partial transformation) or within the defect-free fcc crystal (after full transformation). Thus, the spall strength increases with the fcc phase fraction near the plane of maximum tension. An amorphous microstructure is observed around the voids, likely due to significant heating upon severe plastic deformation, in consistence with experimental clues from the literature. [e-mail : nourou.amadou@ensma.fr and resseguier@ensma.fr]

1. Introduction

Despite extensive research work, both experimental and numerical, the details of polymorphic transformations occurring in shock-loaded iron [1-11], their coupling with the high strain rate elastic-plastic behavior under both compression and release, and their influence on spall damage upon dynamic tension are not fully elucidated yet. While laser-driven compression now allows both shock and ramp loading at extreme strain rates as high as 10^9 s^{-1} [12-15], sometimes combined with ultra-fast in-situ probing of the crystal structure [16-20], Molecular Dynamics (MD) simulations provide complementary insight into the mechanisms governing the evolution of this structure at the atomic scale, over short timescales well-suited to shock physics [21-32]. In recent years, both approaches have brought significant progress towards understanding the response of iron to dynamic compression, including the kinetics of the bcc-hcp transition [33-38], its governing mechanism [18,39], and its strong and complex coupling with highly rate-dependent plasticity [40-46]. Phase-field, energy-based theoretical models have also addressed the formation of different hcp variants and their detailed effects on stress wave propagation [47, 48]. However, the phase transformations occurring within the release wave following the compression front, then upon dynamic tension due to the interaction of this unloading wave with the rarefaction wave reflected from the free surface are still much less documented, although they are likely to play major roles on subsequent spall fracture. In this paper, we use MD simulations to investigate, at the atomic scale, the detailed evolution of shock-loaded single crystal iron during the complete dynamic sequence from shock compression, pressure release, tensile loading, to the nucleation and growth of spall damage.

2. Methods and computational details

Non Equilibrium Molecular Dynamics (NEMD) simulations are performed in [001]-oriented single crystal iron. Samples of 8 million atoms with a 28.7 nm × 28.7 nm section (100 a_0 × 100 a_0 where a_0 is the lattice parameter) and length of 115 nm (400 a_0) were thermalized at 50 K before being shock-compressed along the [001] crystallographic orientation. This sample size was chosen based on previous work with similar loading conditions where it was checked that increasing the sample size to 250×250×400 a_0^3 (about 50 million atoms) did not affect the material response [41].

The thermomechanical behavior of materials is known to be sensitive to pre-existing "defects" in their microstructure [9, 18, 24, 26, 49-51]. For instance, MD simulations have shown the significant influences of nano-voids (i.e. atom vacancies) and grain boundaries on the elastic-plastic response of dynamically compressed iron and subsequent phase transformations [42, 45]. Lattice defects may obviously play major roles in the nucleation of spall damage too. However, in this study, initial samples are perfect single crystals, as a first step to characterize the governing micro-processes and their coupling at the atomic scale.

The simulations were realized using the Large-scale Atomic/Molecular Massively Parallel Simulator (Lammps) molecular dynamics code [52]. There are currently various many-body interatomic potentials to model interactions between atoms in molecular dynamics simulations of iron, including embedded-atom-models (EAM) [53], modified embedded atom models (MEAM) [54], bond order such as the Tersoff model [55], reactive force field (REAXFF) [56], machine-learning (ML-IA) [57-59] or machine learning angular-dependent (ADP) [60]. However, for investigating iron properties under extreme conditions of pressure and deformation, there are relatively few choices providing a reasonable agreement with experiment: the Voter–Chen potential [8], the modified analytic embedded-atom-model [36] and the modified version of the Ackland potential [61]. All these potentials successfully predict the expected hcp phase. However, to our knowledge, the latter, which physical quality has been discussed extensively by Gunkelmann et al. [61, 34], is the only one to account for both plasticity and polymorphism of iron under extreme conditions. Indeed, it predicts the bcc to hcp phase transition at 13.75 GPa under hydrostatic compression [61], in very good agreement with the experimental data [1-3], and relevant plastic deformation in both single crystal [41-43, 45, 46] and polycrystalline iron [34, 35]. This modified version of the Ackland potential is used here.

Shock loading is applied on the sample surface by driving an effective infinite-mass wall piston with an imposed velocity U_p(t) along the Z-direction, while periodic boundary conditions are applied in the transverse directions. The piston velocity is set to a constant value U_p between 800 and 1200 m/s during 10 ps, then drops to zero. The loading strain rates are about 10^9 s^{-1} while strain rates during dynamic tension are on the order of 10^{10} to $10^{11}s^{-1}$ as detailed further. Local thermodynamic and mechanical variables such as mean pressure P_m, longitudinal stress P_z, temperature, etc. are evaluated within a spatial planar bin (of width 3 a_0) perpendicular to the shock wave propagation direction in the same manner as in our previous work [41-43, 46]. Finally, local phases and defects are analyzed by Polyhedral Template Matching (PTM), Centrosymmetry, Dislocation Analysis tool (DXA) and Construct Surface Mesh (CSM), as implemented in the OVITO software [62].

3. Shock compression and unloading

Fig. 1 shows the shock wave propagation along the loading direction for two representative cases where U_p = 800 m/s and 1000 m/s, respectively. For the U_p=800 m/s case (Fig. 1a), the wave structure upon compression was already documented elsewhere [41]. Here, we briefly recall the essential features for completeness, with a focus on the phase transition kinetics. For this lower piston velocity, the maximum mean pressure P_m is about 43 GPa ($P_z \approx$ 48 GPa) enough to drive the bcc-hcp phase transition. Thus, the initially steep compression front splits into two waves (since the elastic wave is overdriven [25]), namely the P_1 wave in which bcc iron undergoes both elastic and plastic deformation and the P_2 wave which drives the bcc to hcp phase transformation (see Fig. 2). The pressure at the top of the P_1 wave corresponding to the structural phase transformation onset pressure is about 28 GPa ($P_z \approx$ 29 GPa), in agreement with results reported under experimental laser compression in iron at ultra-high strain rate [14, 33, 37, 38]. Then, upon further propagation the P_1 wave relaxes to about 26 GPa ($P_z \approx$ 27 GPa), due to kinetics effect governed by the nucleation and growth of the hcp nuclei within the bcc matrix leading to a phase transformation front where both bcc and hcp coexist [33, 37, 38]. For the U_p =1000 m/s case (Fig. 1b), corresponding to a loading pressure P_m of about 53 GPa ($P_z \approx$ 60 GPa), both elastic and P_1 waves are overdriven, so that a steady, single shock front is observed (Fig. 1b), taking almost instantaneously iron from the bcc to hcp phase across a planar interface that propagates toward the sample free surface (see Fig. 3), without distinct nucleation and growth nor kinetics effects.

When the piston is stopped after 10 ps, an incident release wave is initiated which propagates to the right and unloads the material to ambient pressure.

Fig. 2 and Fig. 3 show microstructure evolution in the hcp phase during the compression and

release regimes. In both cases, the evolving microstructure shows twinned variants of the hcp phase (orange) and grain boundaries (yellow) whose aspect depends on the piston velocity. For U_p = 800 m/s, the microstructure in the hcp phase during loading and unloading regimes remains almost the same (Fig. 2). On the other hand, for the U_p = 1000 m/s case, it evolves from small elongated grains of random orientations (inset 1) to larger, parallel grains (inset 3) upon pressure unloading. After full pressure release, the sample returns entirely to the bcc phase with no defects other than randomly distributed point defects.

For all the piston velocities investigated here, the initially sharp release front splits into two waves: the upper part (unloading of the hcp phase) spreads with increasing propagation distance, as expected and usually observed in most materials due to the decrease of sound velocity with pressure, but it is followed by a steep pressure drop. This unusual behavior known as rarefaction shock wave [63] is due to the reverse hcp-bcc transformation, occasioning an anomalous variation of the sound velocity [63-65]. It is consistent with the original theoretical prediction by Drummond [66] later confirmed by early shock experiments under both explosive [67, 68] and plate impact loading conditions [2]. Fig. 2 and Fig. 3 confirm that this sharp release front coincides with the reverse transition from hcp (violet color) back to bcc, after the gradual unloading of the hcp phase.

Another well-known characteristic of the iron bcc-hcp martensitic phase transformation is the existence of a hysteresis between the direct and reverse phase transformations [69, 70]. Accounting for this hysteresis is crucial in determining the dynamic shift of the bcc-hcp phase boundary at ultra-high strain rates compared with the equilibrium phase diagram of iron. In our simulations, the rarefaction shock wave associated with the beginning of the reverse hcp-bcc phase transformation is observed at P_m of about 24 GPa ($P_z \approx$23 GPa), lower than the onset pressure of the direct transformation (about 28 GPa, as mentioned above), which is consistent with the expected hysteresis. The reverse transformation is observed to occur through a rough interface between twinned hcp and high pressure bcc, which propagates forward along with the release front (Fig. 2 and 3). Across this interface, of typical width about 20 a_0, the bcc and hcp are mixed. When pressure falls below ~21 GPa, the hcp phase is found to form a laminar structure within the bcc matrix before complete reversion to bcc [71]. No significant dependence of the reverse phase transformation kinetics on the shock strength was observed. All these results are remarkably consistent with the predictions of a thermomechanic model involving a first-principles DFT-based multi-well energy function for bcc and hcp iron [5]. Quantitatively, the difference between the direct and reverse phase transformation onset stress P_z is about 6 GPa, in fair agreement with the 4-5 GPa hysteresis reported from shock compression experiments [72]. This hysteresis is thought to depend on the degree of completion of the phase transformation [72]. It is found to be roughly independent on the piston velocity in our simulations, since the transition was more than 80% completed in all investigated cases. The mean pressure between the forward and reverse phase transition $P_0 = 1/2(P_{bcc-hcp} + P_{hcp-bcc})$ is 25 GPa, higher than reported at lower strain rate [2], which confirms that ultra-high strain rates can significantly shift the boundary between the bcc and hcp phases, as observed experimentally [14,15, 33, 37, 38].

4. Response to tensile loading

When the compression front (either the P_1 wave for lower piston velocity or the single shock front in case of high piston velocity) reaches the sample free surface, it is reflected into a rarefaction wave propagating from right to left. As this reflected wave meets the incident unloading wave inside the sample, a tensile pulse (negative pressure) is produced. The shape of this pulse and its width are governed by the interactions of the different waves beneath the free surface, which depend on the loading conditions. As discussed above, the unloading wave starts with the gradual release of the hcp phase followed by a rarefaction shock.

For the U_p = 800 m/s case, the reflected release wave results from a complex process, including reverberations of the P_1 wave between the free surface and the oncoming P_2 wave. Its interaction with the incident release wave leads to a wide, nearly Gaussian tensile profile (Fig. 4a). The tensile deformation rate $\dot{\varepsilon}$ at this plane of maximum tension is evaluated at about $7 \times 10^{10}\ s^{-1}$ from the particle velocity spatial profile, following [24, 46]. In many shock experiments, a rough estimate of this tensile rate is classically inferred from time-resolved measurements of the free surface velocity [73, 74]. Here, this estimate, based on the free surface velocity profile in the simulation, is found to be approximately

one order of magnitude lower than the value given above. Both approaches are detailed in Section 4 of the Supplemental Material [75]. The microstructure in this region under tension (Fig. 4b) is mainly composed of twinned variants of the bcc phase with a significant fraction of new fcc phase, up to 50 % in the plane of maximum tension [76]. The fcc phase primarily nucleates at bcc twin boundaries and then grows at the expense of the bcc phase when tension increases. No significant dislocation activities were detected at this stage of tension.

For the U_p = 1000 m/s case (Fig. 5), the single shock front reaching the free surface (Fig. 3) reflects as a single rarefaction wave, which evolves into a gradual release of the hcp phase followed by a sharp release during its backward propagation, just like the incident unloading wave. Wave interactions inside the sample then produce a tensile pulse of "Y-like" shape with a narrow hole of sharper edges and amplitude about 20 GPa (Fig. 5a), slightly higher than in the previous case. Here, the maximum tensile rate $\dot{\varepsilon}$ is about 1×10^{11} s^{-1}. The bcc-fcc phase transformation is completed to more than 95 % phase fraction (see Supplemental Material). Such extensive bcc-fcc phase transformation under a tensile pressure P_m close to 19 GPa is fully consistent with very recent experimental observation under sub-nanosecond laser compression [15].

Fig. 6 shows a detail extracted from a snapshot at 29 ps in the simulation of Fig. 5, showing the fcc arrangement resulting from the bcc-fcc transition observed under dynamic tension along the Z direction. The X, Y, Z axes are the [100], [010], [001] orientations of the initial bcc crystal, respectively. The fcc cell is displayed as colored atoms. While its [001] orientation (green dotted line) still matches the X axis, its [110] orientation (blue dotted line) is parallel to the Z axis. Equivalently, the [011] direction in the parent bcc is the [100] orientation in the daughter fcc. Thus, this bcc-fcc transition is consistent with the Bain transformation path [77]. Note that it is not observed for tensile loading along other low-crystallographic index orientation such as the [110] and [111] orientations.

5. Spall damage

If the tensile load detailed in the above section exceeds the tensile strength of the material, spall damage is expected to occur within the sample, through the nucleation, growth and coalescence of micro-voids or micro-cracks [78, 79]. This well-known dynamic process has been the subject of extensive research work, including MD simulations [80-86]. It depends intimately on the nature of the material (ductile or brittle), the sample microstructure (defects, inclusions, grain boundaries…), the initial conditions (temperature), the thermomechanical history before failure (including phase changes), and the loading rate [73].

As discussed above, the tensile pulse is observed to vary from near Gaussian to a more intense and narrow profile when U_p is increased from 800 to 1000 m/s. This results in a significantly different microstructure at the plane of maximum tension, namely twinned bcc mixed with fcc for the lower piston velocity versus defect-free fcc single crystal for the higher piston velocity (Figs. 4, 5, 7). In both cases, voids start to nucleate (Fig. 7), which means the local tension P_m (negative pressure) overcomes the tensile strength of the material. Such nucleation and subsequent growth of stable voids create new free surfaces allowing progressive relaxation of the tensile stress through two recompression fronts that propagate from the spall plane in opposite directions (Fig. 8). Thus, the spall strength is given by the minimum pressure P_m (negative in tension) computed where voids nucleate (at the so-called spall plane).

In both plate impact experiments [64, 67, 68] and laser shock experiments [87], post-recovery observations of spalled samples have evidenced a drastic change from a rough fracture surface morphology in bcc-iron to a so-called "smooth spall" after the bcc-hcp-bcc cycle, partially attributed to the highly localized tension resulting from the interaction of two rarefaction shock waves due to the reverse hcp-bcc transition. Here (and in Fig. 11 further), the fracture surface does not appear particularly smooth, but it corresponds to an extremely early stage of damage development (a few ps) and tiny spatial scales (a few nm). Thus, it would obviously take a much larger sample and a much longer simulation time to discriminate the different morphologies reported in the experiments.

For U_p = 800 m/s (Fig. 7a), the voids are found to nucleate either at twins boundaries or at fcc-bcc phase boundaries (Fig. 9), which constitute weak sites favoring damage activation, in consistence with previous work [88].

For U_p = 1000 m/s (Fig. 7b), voids are observed to nucleate within the fcc crystal, where the

absence of preferential fracture sites results in a higher spall strength. Thus, the maximum tensile stress induced at the spall plane is found to increase from 17.1 to 21.9 GPa upon increasing piston maximum velocity from 800 to 1200 m/s, which points to a strong correlation between the spall strength and the maximum fcc phase fraction (Fig. 10). This is consistent with recent data reported by Ma and Dongare [86], shown in the same plot (discrepancies come mainly from different initial sample temperatures, 50 K *vs*. 300 K, and different tools to analyze phase fractions, PTM *vs*. CNA). Because the amount of fcc phase was shown to depend directly on the tensile rate and on the loading pressure (see Section 4 and Fig. 10), this correlation evidenced at the atomic scale may provide new insight to interpret the variations of spall strength observed experimentally in shock-loaded iron [6, 65, 73, 87-89].

Void growth is accompanied by intense plastic deformation nearby, which is found to be accommodated by the emission, multiplication and propagation of dislocations, either lines or loops (Fig. 11). These dislocations are composed mainly of ½<111> type with a local screw character. Thus, the observed dislocations loops are composed of two screw dislocations with a leading edge local character. These loops expand until they meet defects such as twin boundaries. The dislocation density increases up to 5×10^{12}cm^{-2} for the U_p = 1000 m/s case. Subsequent dissipation induces strong local heating, with a temperature as high as 2000 K [90], which is observed to result in a complex microstructure including amorphous regions around void (Fig. 12).

Fig. 13 shows the free surface velocity profiles for three values of the piston velocity. In all cases, this imposed piston velocity coincides necessarily with the particle velocity U_p behind the compression front. After a transit time slightly dependent on loading pressure, shock breakout produces a steep acceleration to a peak velocity. In case of a single shock front (high piston velocities), this peak free surface velocity is twice U_p, which matches a classical approximation in shock physics [2, 63]. For the lowest piston velocity (U_p = 800 m/s), the incident wave-front is split into a double structure (P_1 wave followed by P_2, see Section 3), so that this approximation is no longer valid and the maximum free surface velocity is 1470 m/s, lower than $2\times U_p$. Next, the emergence of the unloading wave at the free surface produces a gradual deceleration, interrupted by a reacceleration (around 40 ps) usually referred to as the spall pulse, due to the arrival of the relaxation wave generated at the spall plane upon void opening (see Fig. 8). Thereafter, wave reverberation across the "spall", i.e. between the spall plane and the free surface, produces velocity oscillations. Hence, the period of these oscillations, about 13.5 ps here, should be twice the transit time across the "spall" thickness (because waves propagate back and forth). Assuming a mean propagation velocity at the bulk sound speed of iron C_0 = 4640 m/s [89], this theoretical thickness would then be about 31.3 nm, which agrees very well with the distance between the fracture plane and the free surface evaluated to 32 nm in the snapshots (see e.g. Fig. 9 and 11). Finally, using the so-called acoustic approximation, the amplitude ΔU of the deceleration from the peak velocity to the minimum just before the spall pulse, usually called the velocity pullback, provides an estimate of the tensile strength [78, 79], $\sigma_R = ½\ \rho_0\ C_0\ \Delta U$, where ρ_0 is the initial density. This classic relationship is widely used to interpret velocity records in experiments [e.g. 74, 89], and it has been discussed in molecular dynamics too [82]. The σ_R estimates thus obtained vary between about 22 to 24 GPa depending on the piston velocity [91]. They are systematically higher by about 10 to 20% than the maximum tension calculated at the spall plane before void opening and subsequent relaxation (spall strength values in Fig. 10). Such discrepancy is probably due to the limits of the rough and simple relationship recalled above.

6. Conclusion

NEMD simulations were used to investigate phase transformations and plasticity in shock-loaded single crystal iron with a specific attention to the unloading wave, its interaction with the reflected rarefaction wave, and how subsequent spall damage depends on the various, highly coupled processes occurring during the full sequence. Shock pressure was varied to investigate both the double-structure and overdriven regimes, which were shown to lead to significantly different responses. Upon unloading, the reverse hcp-bcc phase transition starts at about 23 GPa, with an hysteresis between the direct and reverse transformations and the propagation of a rarefaction shock, in fair agreement with experimental data. The mean pressure between the forward and reverse phase transition is observed to be higher than

reported at lower strain rate, which confirms that ultra-high strain rates can significantly shift the boundary between the bcc and hcp phases, as observed experimentally. Next, the tensile pulse produced by release wave interaction, which shape and intensity depend on shock pressure, is found to induce a bcc to fcc phase transformation beyond a tensile pressure of about 19 GPa, consistent with recent experimental observation under sub-nanosecond laser-driven compression. The mechanism governing this polymorphic transition is consistent with the Bain transformation path. Subsequent spall damage starts with the nucleation of roughly spherical voids, either at favorable sites (twin and grain boundaries, bcc-fcc interfaces) or within the bulk of fcc crystal in the absence of such sites after complete transformation under high tension. As a consequence, the spall strength increases with the fcc phase fraction near the plane of maximum tension. Finally, the later stage of void growth and coalescence involves intense, dislocation-mediated plasticity leading to large dissipation and strong local heating, which results in amorphous regions around the voids.

This detailed analysis at the atomic scale provides a data basis which may allow better interpretations of a variety of experimental observations, both past and future.

Acknowledgments

This work was partially funded by the French Program CNRS-Africa..Computations were performed on the supercomputer facilities of the Mésocentre de calcul de Poitou Charentes (France). We thank Mikaël Gueguen and Gérald Sailly (Institut Pprime) for their kind help to set up workstations and access. We also deeply thank André Dragon for thoughtful discussions and critical comments on the manuscript, as well as for his continued support over the past six years.

References

[1] D. Bancroft, E. L. Peterson, and S. Minshall, Polymorphism of Iron at High Pressure, J. Appl. Phys. **27**, 291 (1956).

[2] L. M. Barker and R. E. Hollenbach, Shock wave study of the α-ε transition in iron, J. Appl. Phys. **45**, 4872–4887 (1974).

[3] J. C. Boettger and D. C. Wallace, Metastability and dynamics of the shock-induced phase transition in iron, Phys. Rev. B **55**, 2840–2849 (1997).

[4] A. Lew, K. Caspersen, E.A. Carter, and M. Ortiz, Quantum mechanics based multiscale modeling of stress-induced phase transformations in iron, J. Mech. Phys. Solids **54**, 1276-1303 (2006).

[5] K. J. Caspersen, A. Lew, M. Ortiz, and E. A. Carter, Importance of shear in the bcc-to-hcp transformation in iron, Phys. Rev. Lett. **93**,115501 (2004).

[6] E. B. Zaretsky, Shock response of iron between 143 and 1275 K, J. Appl. Phys. **106**, 023510 (2009).

[7] K. Kadau, T. C. Germann, P. S. Lomdahl, and B. L. Holian, Microscopic View of Structural Phase Transitions Induced by Shock Waves, Science **296**, 1681 (2002).

[8] K. Kadau, T. C. Germann, P. S. Lomdahl, and B. L. Holian, Atomistic simulations of shock-induced transformations and their orientation dependence in bcc Fe single crystals, Phys. Rev. B **72**, 064120 (2005).

[9] K. Kadau, T. C. Germann, P. S. Lomdahl, R. C. Albers, J. S. Wark, A. Higginbotham, and B. L. Holian, Shock Waves in Polycrystalline Iron, Phys. Rev. Lett. **98**, 135701 (2007).

[10] B. Dupré, B. Amadon, Y.-P. Pellegrini, and C. Denoual, Mechanism for the α→β phase transition in iron, Phys. Rev. B **87**, 024103 (2013).

[11] N. A. Zarkevich and D. D. Johnson, Coexistence pressure for a martensitic transformation from theory and experiment: Revisiting the bcc-hcp transition of iron under pressure, Phys. Rev. B. **91**, 174104 (2015).

[12] J.C. Crowhurst, M. R. Armstrong, K.B. Knight, J. M. Zaug, and E. M. Behymer, Invariance of the Dissipative Action at Ultrahigh Strain Rates Above the Strong Shock Threshold. Phys. Rev. Lett. **107**, 144302 (2011).

[13] N. Amadou, E. Brambrink, A. Benuzzi-Mounaix, G. Huser, F. Guyot, S. Mazevet, G.

Morard, T. de Rességuier, T. Vinci, K. Myanishi, N. Ozaki, R. Kodama, T. Boehly, O. Henry, D. Raffestin, and M. Koenig, Direct laser-driven ramp compression studies of iron: A first step toward the reproduction of planetary core conditions, High Energy Density Physics, **9**, 243 (2013).

[14] J.C. Crowhurst, B. W. Reed, M. R. Armstrong, H. B. Radousky, J. A. Carter, D. C. Swift, J.M. Zaug, R. W. Minich, N. E. Teslich, and M. Kumar, The phase transition in iron at strain rates up to 10^9 s^{-1}, J. Appl. Phys. **115**, 113506 (2014).

[15] H. Hwang, E. Galtier, H. Cynn, I. Eom, S.H. Chun, Y. Bang, G.C. Hwang, J. Choi, T. Kim, M. Kong, et al., Subnanosecond phase transition dynamics in laser-shocked iron. Sci. Adv. **6**, 5132 (2020).

[16] D. H. Kalantar, J. F. Belak, G. W. Collins, J. D. Colvin, H. M. Davies, J. H. Eggert, T. C. Germann, J. Hawreliak, B. L. Holian, K. Kadau, P. S. Lomdahl, H. E. Lorenzana, M. A. Meyers, K. Rosolankova, M. S. Schneider, J. Sheppard, J. S. Stölken, and J. S. Wark, Direct Observation of the α-ε transition in Shock-Compressed Iron via Nanosecond X-Ray Diffraction, Phys. Rev. Lett. **95**, 075502 (2005).

[17] B. Yaakobi, T. R. Boehly, D. D. Meyerhofer, T. J. B. Collins, B. A. Remington, P. G. Allen, S. M. Pollaine, H. E. Lorenzana, and J. H. Eggert, EXAFS Measurement of Iron bcc-to-hcp Phase Transformation in Nanosecond-Laser Shocks, Phys. Rev. Lett. **95**, 075501 (2005).

[18] J. Hawreliak, J. D. Colvin, J. H. Eggert, D. H. Kalantar, H. E. Lorenzana, J. S. Stölken, H. M. Davies, T. C. Germann, B. L. Holian, K. Kadau, P. S. Lomdahl, A. Higginbotham, K. Rosolankova, J. Sheppard, and J. S. Wark, Analysis of the x-ray diffraction signal for the α-ε transition in shock-compressed iron: Simulation and experiment, Phys. Rev. B **74**, 184107 (2006).

[19] G. Aquilanti, A. Trapananti, A. Karandikar, I. Kantor, C. Marini, O. Mathon, S. Pascarelli, and R. Boehler, PNAS, **112**, 12042–12045 (2015).

[20] A. Denoeud, N. Ozaki, A. Benuzzi-Mounaix, H. Uranishi, Y. Kondo, R. Kodama, E. Brambrink, A. Ravasio, M. Bocoum, J.-M. Boudenne, et al. Dynamic X-ray diffraction observation of shocked solid iron up to 170 GPa, PNAS **13**, 7745-7749 (2016).

[21] B.L. Holian and P.S. Lomdahl, Plasticity induced by shock waves in nonequilibrium molecular-dynamics simulations, Science **280**, 2085–2088 (1998).

[22] T.C. Germann, B.L. Holian, P.S. Lomdahl, and R. Ravelo, Orientation dependence in molecular dynamics simulations of shocked single crystals, Phys. Rev. Lett. **84**, 5351–5354 (2000).

[23] E.M. Bringa, K. Rosolankova, R.E. Rudd, B.A. Remington, J.S. Wark, M. Duchaineau, D.H. Kalantar, J. Hawreliak, and J. Belak, Shock deformation of face centred-cubic metals on subnanosecond timescales, Nat. Mater. **5**, 805-809 (2006).

[24] X. Cui, W. Zhu, H. He, X. Deng, and Y. Li, Phase transformation of iron under shock compression: effects of voids and shear stress, Phys. Rev. B **78**, 024115 (2008).

[25] R. Ravelo, T. C. Germann, O. Guerrero, Q. An, and B. L. Holian. Shock-induced plasticity in tantalum single crystals: Interatomic potentials and large-scale molecular-dynamics simulations, Phys. Rev. B **88**,134101 (2013).

[26] L.A. Zepeda-Ruiz, A. Stukowski, T. Oppelstrup, and V.V. Bulatov, Probing the limits of metal plasticity with molecular dynamics simulations, Nature **550**, 492 (2017).

[27] H. T. Luu, R. J. Ravelo, M. Rudolph, E. M. Bringa, T. C. Germann, D. Rafaja, and N. Gunkelmann, Shock-induced plasticity in nanocrystalline iron: Large-scale molecular dynamics simulations, Phys. Rev. B **102**, 20102 (2020).

[28] P. Wen, B. Demaske, D. E. Spearot, S. R. Phillpot, and G. Tao, Effect of the initial temperature on the shock response of $Cu_{50}Zr_{50}$ bulk metallic glass by molecular dynamics simulation, J. Appl. Phys. **129**, 165103 (2021).

[29] C. A. Duarte, C. Li, B. W. Hamilton, A. Strachan, and M. Koslowski, Continuum and molecular dynamics simulations of pore collapse in shocked ***β***-tetramethylene tetranitramine (***β***-HMX) single crystals, J. Appl. Phys. **129**, 015904 (2021).

[30] B. W. Hamilton, M. N. Sakano, C. Li, and A. Strachan, Chemistry under shock conditions, Annu. Rev. Mater. Res. **51**, 101 (2021).

[31] P. Wen, G. Tao, D. E. Spearot, and S.R. Phillpot, Molecular dynamics simulation of the

shock response of materials: a tutorial, J. Appl. Phys. **131**, 051101, (2022).
[32] Y. Tu, M. Fang, T. Guo, T. Wang, L. Yuan, P. Shi, G. Sas, L. Elfgren, Shock-induced reactive molecular dynamics simulation in sodium aluminosilicate hydrate: wave propagation, mechanical response, and structural deformation, Journal of Non-Crystalline Solids **612**, 122350 (2023).
[33] R. F. Smith, J. H. Eggert, D. C. Swift, J. Wang, T. S. Duffy, D. G. Braun, R. E. Rudd, D. B. Reisman, J.-P. Davis, M. D. Knudson, and G. W. Collins, Time-dependence of the alpha to epsilon phase transformation in iron. J. Appl. Phys. **114**, 223507 (2013).
[34] N. Gunkelmann, E. M. Bringa, D. R. Tramontina, C. J. Ruestes, M. J. Suggit, A. Higginbotham, J. S. Wark, and H. M. Urbassek, Shock waves in polycrystalline iron: Plasticity and phase transitions. Phys. Rev. B **89**, 140102, (2014).
[35] N. Gunkelmann, D. R. Tramontina, E. M. Bringa, and H. M. Urbassek, Interplay of plasticity and phase transformation in shock wave propagation in nanocrystalline iron, New J. Phys. **16**, 093032 (2014).
[36] K. Wang, S. Xiao, H. Deng, W. Zhu, and W. Hu, An atomic study on the shock-induced plasticity and phase transition for iron-based single crystals, Int. J. Plasticity **59**, 180-198 (2014).
[37] N. Amadou, E. Brambrink, A. Benuzzi-Mounaix, G. Huser, F. Guyot, S. Mazevet, G. Morard, T. de Rességuier, T. Vinci, K. Myanishi, N. Ozaki, R. Kodama, T. Boehly, O. Henry, D. Raffestin, and M. Koenig, Kinetics of the iron α-ε phase transition at high-strain rates: Experiment and model, Phys. Rev. B **93**, 214108 (2016)
[38] N. Amadou, E. Brambrink, T. de Rességuier, A. O. Manga, A. Aboubacar, B. Borm, and A. Molineri, Laser-driven ramp compression to investigate and model dynamic response of iron at high strain rates, Metals **6**, 320 (2016).
[39] H.E. Lorenzana, J.F. Belak, K.S. Bradley, E.M. Bringa, K.S. Budil, J.U. Cazamias, B. El-Dasher, J. A. Hawreliak, J. Hessler, K. Kadau, D.H. Kalantar, J.M. McNaney, D. Milathianaki, K. Rosolankova, D.C. Swift, M. Taravillo, T.W.V. Buuren, J.S. Wark, and T.D. de la Rubia, Shocked materials at the intersection of experiment and simulation, Sci. Model Simul. **15**, 159-186 (2008).
[40] K. Wang, W. Zhu, S. Xiao, K. Chen, H. Deng, and W. Hu, Coupling between plasticity and phase transition of polycrystalline iron under shock compressions, Int. J. Plasticity **71**, 218 (2015).
[41] N. Amadou, T. de Rességuier, A. Dragon, and E. Brambrink. Coupling between plasticity and phase transition in shock- and ramp-compressed single-crystal iron, Phys. Rev. B **98**, 024104, (2018).
[42] N. Amadou, T. de Rességuier, A. Dragon, and E. Brambrink. Effects of orientation, lattice defects and temperature on plasticity and phase transition in ramp-compressed single crystal iron, Comput. Mater. Sci. **172**, 109318 (2020).
[43] N. Amadou, T. de Rességuier, and A. Dragon. Coupling between plasticity and phase transition in single crystal iron at ultra-high strain rate. AIP Conf. Proc. **2272**, 070001 (2020).
[44] J.-L. Shao, W. He, T. Xi, and J. Xin, Microscopic insight into the structural transition of single crystal iron under the ramp wave loading, Comput. Mater. Sci. **182**, 109772 (2020).
[45] N. Amadou, T. de Rességuier, and A. Dragon. Influence of point defects and grain boundaries on plasticity and phase transition in uniaxially-compressed iron. Computational Condensed Matter **27**, e00560 (2021).
[46] N. Amadou, A. R. A. Abdoulaye, T. de Rességuier, A. Dragon, Strain-Rate Dependence of Plasticity and Phase Transition in [001]-Oriented Single-Crystal Iron, Crystals **13**, 250 (2023).
[47] A. Vattré and C. Denoual, Polymorphism of iron at high pressure: a 3D phase-field model for displacive transitions with finite elastoplastic deformations, J. Mech. Phys. Solids **92**, 1-27 (2016).
[48] A. Vattré and C. Denoual, Continuum nonlinear dynamics of unstable shock waves induced by structural phase transformations in iron, J. Mech. Phys. Solids **131**, 387–403 (2019).

[49] H.-T. Luu, R. G. A. Veiga and N. Gunkelmann, Atomistic study of the role of defects on α-ε phase transformations in iron under hydrostatic compression, Metals **9**, 1040 (2019).
[50] H.-T. Luu, N. Gunkelmann, Pressure-induced phase transformations in Fe-C: Molecular dynamics approach, Compt. Mat. Sc. **162**, 295 (2019).
[51] Y. Huang, Y. Xiong, P. Li, X. Li, S. Xiao, H. Deng, W. Zhu, W. Hua, Atomistic studies of shock-induced plasticity and phase transition in iron-based single crystal with edge dislocation, Int. J. Plast. **114**, 215–226 (2019).
[52] S. Plimpton, Fast parallel algorithms for short-range molecular dynamics, J. Comp. Phys., **117**, 1-19 (1995).
[53] M. S. Daw and M. I. Baskes, Semiempirical, quantum mechanical calculation of hydrogen embrittlement in metals, Phys. Rev. Lett. **50**, 1285-1288 (1983).
[54] M.I. Baskes, Modified embedded-atom potentials for cubic materials and impurities, Phys. Rev. B **46**, 2727–2742 (1992).
[55] J. Tersoff, New empirical approach for the structure and energy of covalent systems, Phys. Rev. B, **37**, 6991 (1988).
[56] K.K. Chenoweth, A.C.T. van Duin, W.A. Goddard, ReaxFF Reactive Force Field for Molecular Dynamics Simulations of Hydrocarbon Oxidation, J. Phys. Chem. A **112**, 1040–1053 (2008).
[57] A. P. Bartók, M. C. Payne, R. Kondor, and G. Csányi, Gaussian Approximation Potentials: The Accuracy of Quantum Mechanics, without the Electrons, Phys. Rev. Lett. **104**, 136403 (2010).
[58] A.P. Thompson, L.P. Swilerb, C.R. Trott, S.M. Foiles, G.J. Tucker, Spectral neighbor analysis method for automated generation of quantum-accurate interatomic potentials, J. Comput. Phys. **285**, 316–330 (2015).
[59] R. Jana and M. A. Caro, Searching for iron nanoparticles with a general-purpose Gaussian approximation potential, Phys. Rev. B **107**, 245421 (2023).
[60] S. Starikov, D. Smirnova, T. Pradhan, Y. Lysogorskiy, H. Chapman, M. Mrovec, and R. Drautz, Angular-dependent interatomic potential for large-scale atomistic simulation of iron: Development and comprehensive comparison with existing interatomic models, Phys. Rev. Materials **5**, 063607 (2021).
[61] N. Gunkelmann, E. M. Bringa, K. Kang, G. J. Ackland, C. J. Ruestes, and H. M. Urbassek, Polycrystalline iron under compression: Plasticity and phase transitions. Phys. Rev. B, **86**, 144111 (2012).
[62] A. Stukowski, Visualization and analysis of atomistic simulation data with OVITO-the open visualization tool, Model. Simul. Mat. Sci. Eng. **18,** 015012 (2009).
[63] Ya. B. Zel'dovich and Yu. P. Raizer, Physics of Shock Waves and High-Temperature Hydrodynamic Phenomena, edited by W. D. Hayes and R. F. Probstein, New-York, pp: 685-784 (2002).
[64] J. O. Erkman, Smooth spalls and the polymorphism of iron, J. Appl. Phys. **32,** 939-944 (1961).
[65] E. A. Kozlov, Shock adiabat features, phase transition macrokinetics, and spall fracture of iron in different phase states, High Pres. Res. **10**, 541-582 (1992).
[66] W. E. Drummond. Multiple shock production. J. Appl. Phys. **28**, 998-1001 (1957).
[67] A. G. Ivanov and S. A. Novikov, Rarefaction shock waves in iron and steel, J. Exptl. Theor. Phys. **4**, 1880-1882 (1961).
[68] L. V. Altshuler, R. F. Trunin, V. D. Urlin, V. E. Fortov, and A. I. Funtikov, Development of dynamic high-pressure techniques in Russia. Physics-Uspekhi **42**, 261-280 (1999).
[69] P. M. Giles, M. H. Longenbach, and A. R. Marder. High-pressure martensitic transformation in iron. J. Appl. Phys. **42**, 4290–4295 (1971).
[70] R. D. Taylor, M. P. Pasternak, and R. Jeanloz, Hysteresis in the high pressure transformation of bcc- to hcp-iron, J. Appl. Phys. **69**, 6126-6128 (1991).
[71] See Supplemental Material at [URL to be inserted by the publisher] for a more detailed description of the hcp-bcc reverse transformation upon pressure unloading.
[72] V. D. Blank and E. I. Estrin. Phase Transitions in Solids Under High Pressure, edited by CRC

Press, pp: 166-190 (Boca Raton, FL 2014).
[73] G.I. Kanel, Spall fracture: methodological aspects, mechanisms and governing factors, Int. J. Fract. **163**, 173 (2010).
[74] T. de Rességuier, E. Lescoute, and D. Loison, Influence of elevated temperature on stress wave propagation and spallation in laser shock-loaded iron, Phys. Rev. B **86**, 214102 (2012).
[75] See Supplemental Material at [URL to be inserted by the publisher] for the strain rates inferred from two different methods.
[76] See Supplemental Material at [URL to be inserted by the publisher] for more details on the phase fraction evolutions.
[77] L. H. Zhang, M. J. Cheng, X. H. Shi, J. W. Shuai, and Z. Z. Zhu. Bain and Nishiyama-Wassermann transition path separation in the martensitic transitions of Fe, RSC Adv. **11**, 3043–3048, (2021).
[78] D.E. Grady, The Spall Strength of Condensed Matter, J. Mech. Phys. Solids **36**, 353-384 (1988).
[79] T. Antoun, L. Seaman, D.R. Curran, G.I. Kanel, S.V. Razorenov and A.V. Utkin, Spall Fracture, Springer, New York (2002).
[80] V. V. Stegailov and A.V. Yanilkin, Structural transformations in single-crystal iron during shock-wave compression and tension: molecular dynamics simulation, J. Exp. Theor. Phys. **104**, 928-935 (2007).
[81] Q. An, R. Ravelo, T.C. Germann, W.Z. Han, S.N. Luo, D.L. Tonks and W.A. Goddard, Shock compression and spallation of single crystal tantalum, AIP Conf. Proc. **1426**, 1259 (2012).
[82] N. Gunkelmann, E. M. Bringa, and H. M. Urbassek, Influence of phase transition on shock-induced spallation in nanocrystalline iron, J. Appl. Phys. **118**,185902 (2015).
[83] M. Xiang, J. Chen and R. Su, Spalling behaviors of Pb induced by ramp-wave loading: effects of the loading rise time studied by molecular dynamics simulations, Computational Materials Science **117**, 370–379 (2016).
[84] T. Qiu, Y. Xiong, S. Xiao, X. Li, W. Hu and H. Deng et al., Non-equilibrium molecular dynamics simulations of the spallation in Ni: effects of vacancies, Computational Materials Science **137**, 273–281 (2017).
[85] D. Thürmer, S. Zhao, O.R. Deluigi, C. Stan, I.A. Alhafez, H.M. Urbassek, M.A. Meyers, E.M. Bringa and N. Gunkelmann, J. of Alloys and Compounds **895**, 162567 (2022).
[86] K. Ma and A. M. Dongare, Role of α-ε-α phase transformation on the spall behavior of iron at atomic scales, J. Mater. Sci., **57**, 12556–12571 (2022).
[87] T. de Rességuier and M. Hallouin, Effects of the α-ε phase transition on wave propagation and spallation in laser shock-loaded iron, Phys. Rev. B **77** (17), 174107 (2008).
[88] G. Righi, C. J. Ruestes, C. V. Stan, S. J. Ali, R. E. Rudd, M. Kawasaki, H.-S. Park, and M. A. Meyers, Towards the ultimate strength of iron: spalling through laser shock, Acta Mater. **215**, 117072 (2021).
[89] G. Morard, T. de Rességuier, T. Vinci, A. Benuzzi-Mounaix, E. Lescoute, E. Brambrink, M. Koenig, H.G. Wei, A. Diziere, F. Occelli, G. Fiquet, and F. Guyot, High power laser shock-induced dynamic fragmentation of iron foils, Phys. Rev. B **82**, 174102 (2010).
[90] See Supplemental Material at [URL to be inserted by the publisher] for the temperature evolution at the spall plane.
[91] See Supplemental Material at [URL to be inserted by the publisher] for the spall strength inferred from two different methods.

Figure Captions

Fig. 1. Wave profiles for piston maximum velocity U_p of 800 m/s (a) and 1000 m/s (b) showing a two-wave (a) or single compression front (b), as well as the propagation of a shock upon release (see text for details).

Fig. 2. Mean stress spatial profile (top) at 17 ps for U_p =800 m/s with associated atomic configuration (bottom). Bcc atoms are colored according to local pressure, atoms associated to defects are colored in brown, while hcp and fcc phases are colored in violet and cyan respectively. The insets show the microstructure within sections in the compressed state (1) and during release (2) of the hcp phase.

Fig. 3. Mean stress spatial profile (top) at 17 ps for the piston maximum velocity of 1000 m/s with associated atoms configuration (bottom) where colors meaning is the same as in Fig. 2. The insets show the evolution of the microstructure in the hcp phase from the compressed state (1) to successive stages during the release (2 and 3).

Fig. 4. Mean stress distribution along the Z axis (a) at 31 ps showing tensile (negative pressure) wave spatial profile for the piston velocity of 800 m/s with the corresponding atomic configuration (b). Atoms are colored like in Fig. 2: cyan corresponds to the fcc phase.

Fig. 5. Mean stress distribution at 28 ps (a) showing tensile wave spatial profile for the piston velocity of 1000 m/s with the corresponding atomic configuration (b), where atoms are colored like in Fig.2. An extensive phase transition from the bcc to fcc phase (cyan) is observed under tension.

Fig. 6. Detail extracted from the cyan zone in the simulation of Fig. 5, showing the fcc arrangement resulting from the bcc-fcc transition observed under dynamic tension along the Z direction. The X, Y, Z axes are the [100], [010], [001] orientations of the initial bcc crystal. The fcc cell is displayed as colored atoms. While its [001] orientation (green dotted line) still matches the X axis, its [110] orientation (blue dotted line) is parallel to the Z axis. Equivalently, and given the crystal symmetries, the [011] direction in the parent bcc is the [100] orientation in the daughter fcc (yellow dotted line), so that this bcc-fcc transition is consistent with the Bain transformation path.

Fig. 7. Snapshots at successive times showing voids (forest-green colored surface) nucleation and growth for piston maximum velocity of 800 m/s (a) and 1000 m/s (b).

Fig. 8. Pressure distribution at successive times for piston velocity of 800 m/s (a) and 1000 m/s (b), showing the tensile pulse (negative pressure) induced within the sample (black), then the progressive stress relaxation accompanying the nucleation and growth of spall damage.

Fig. 9. Longitudinal cut within the sample at 33 ps for the 800 m/s piston velocity, showing voids (green colored surface) nucleated mainly at twin boundaries and phase boundaries.

Fig. 10. Spall strength (black) and fcc phase fraction (red) evolution as functions of the maximum shock pressure

Fig. 11. Late-time snapshots showing extensive voids growth and coalescence for piston velocities 800 m/s (a) and 1000 m/s (b), with intense plastic activity in their vicinity, which is found to be dislocation-mediated (green loops in the bottom pictures).

Fig. 12. Snapshots showing the microstructure evolution around the voids (forest-green colored surface) at different simulation times for piston velocity of 800m/s (a) and 1000 m/s (b). Atoms are colored according the local phase structure: bcc, fcc and hcp atoms are blue, cyan and violet, respectively, while

white color represents atoms with no identified local phase structure according to the PTM analysis, i.e. regions which can be considered amorphous.

Fig. 13. Free surface velocity profiles for a piston velocity of 800, 900 and 1000 m/s, respectively.

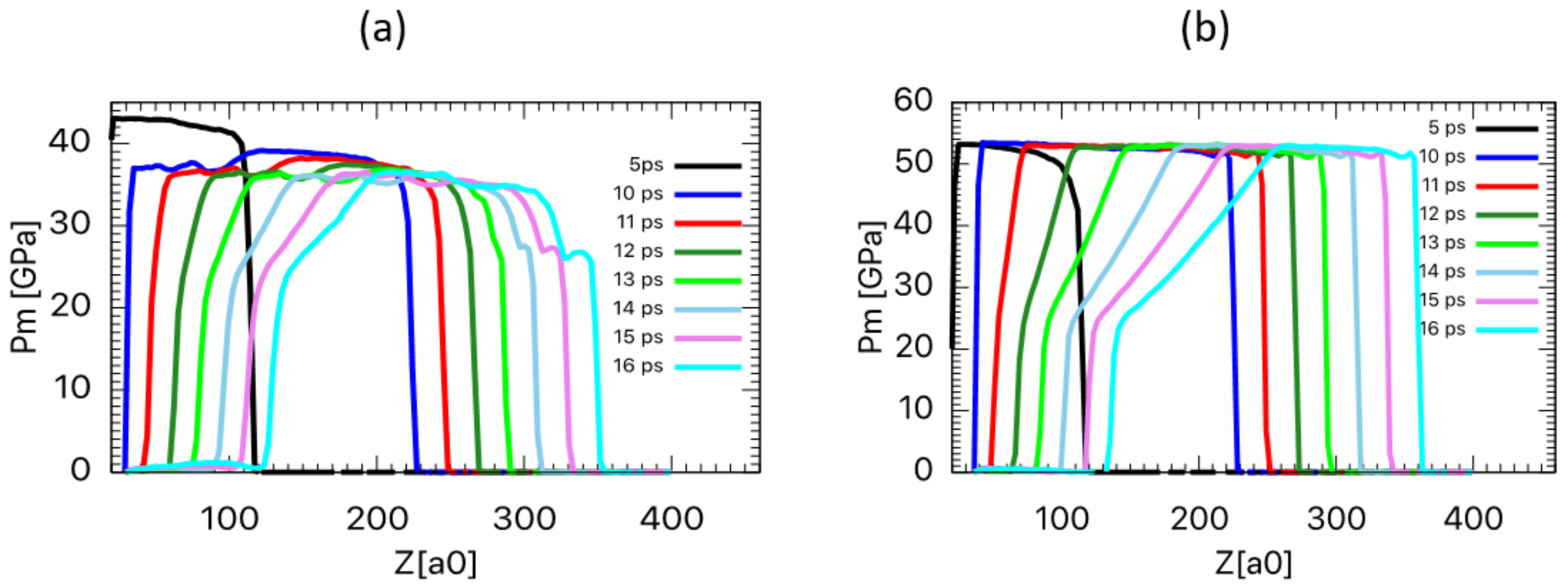
(a)
(b)
Pm [GPa]
Z[a0]
5ps
10 ps
11 ps
12 ps
13 ps
14 ps
15 ps
16 ps
0
10
20
30
40
50
60
100
200
300
400

Z[a0]

0 100 200 300 400

Pm [GPa]

40 30 20 10 0

1

2

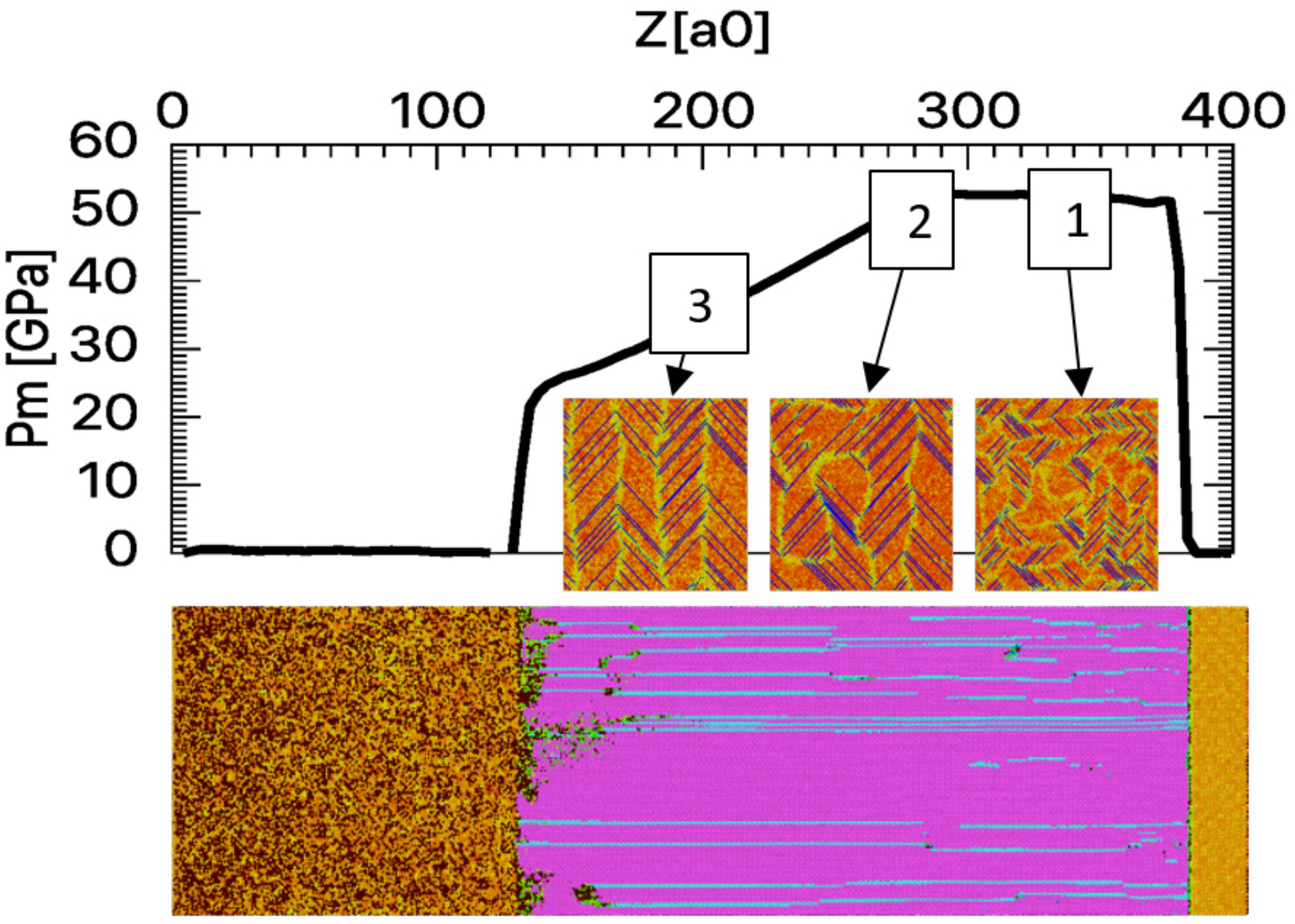
Z[a0]
0
100
200
300
400
Pm [GPa]
60
50
40
30
20
10
0
1
2
3

Z[a0]

0 100 200 300 400 500

5 0 -5 -10 -15 -20

Pm [GPa]

(a)

(b)

31 ps

Pressure scale

0 GPa

-20 GPa

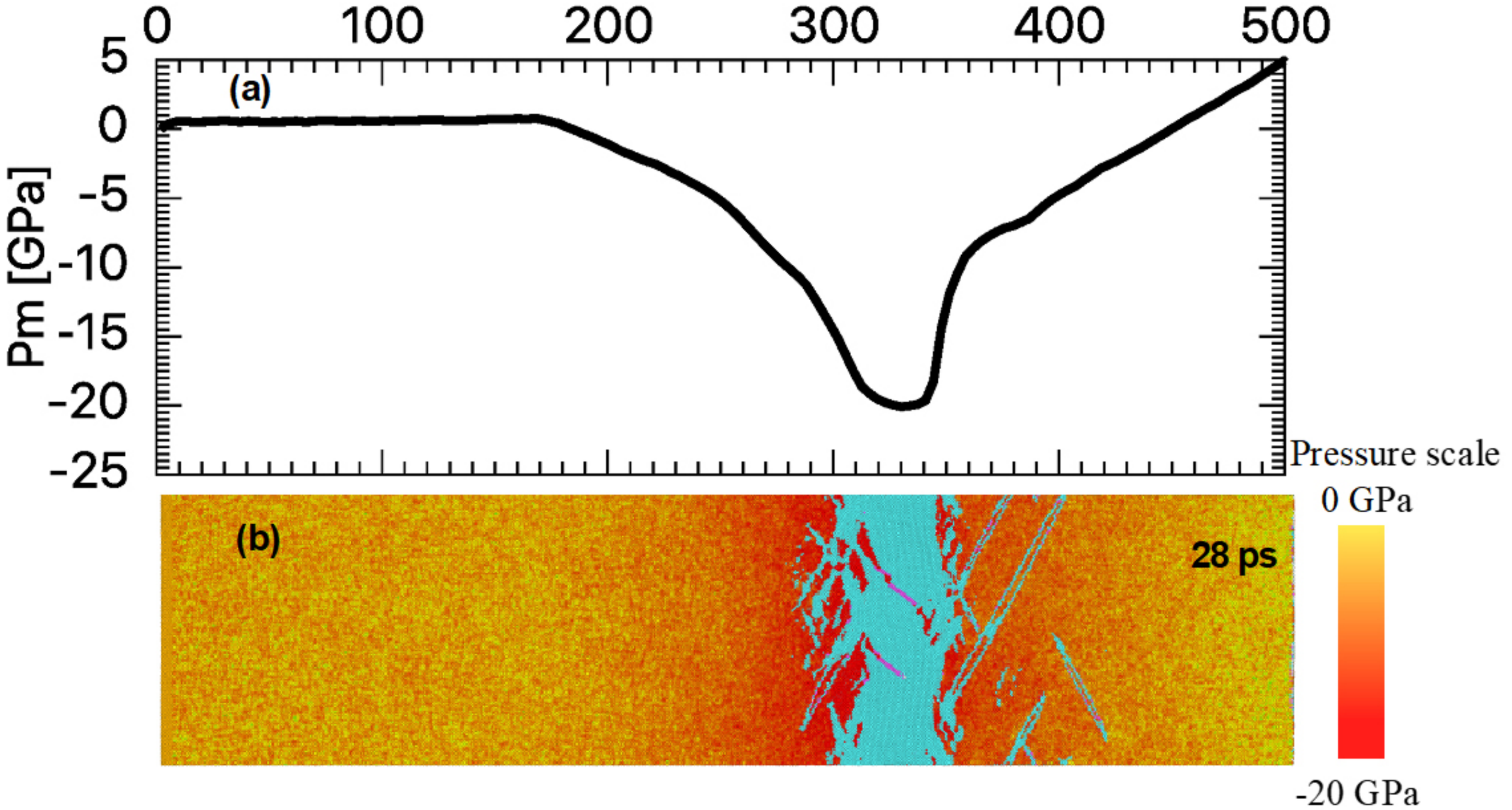
0
100
200
300
400
500
5
0
-5
-10
-15
-20
-25
Pm [GPa]
(a)
(b)
28 ps
Pressure scale
0 GPa
-20 GPa

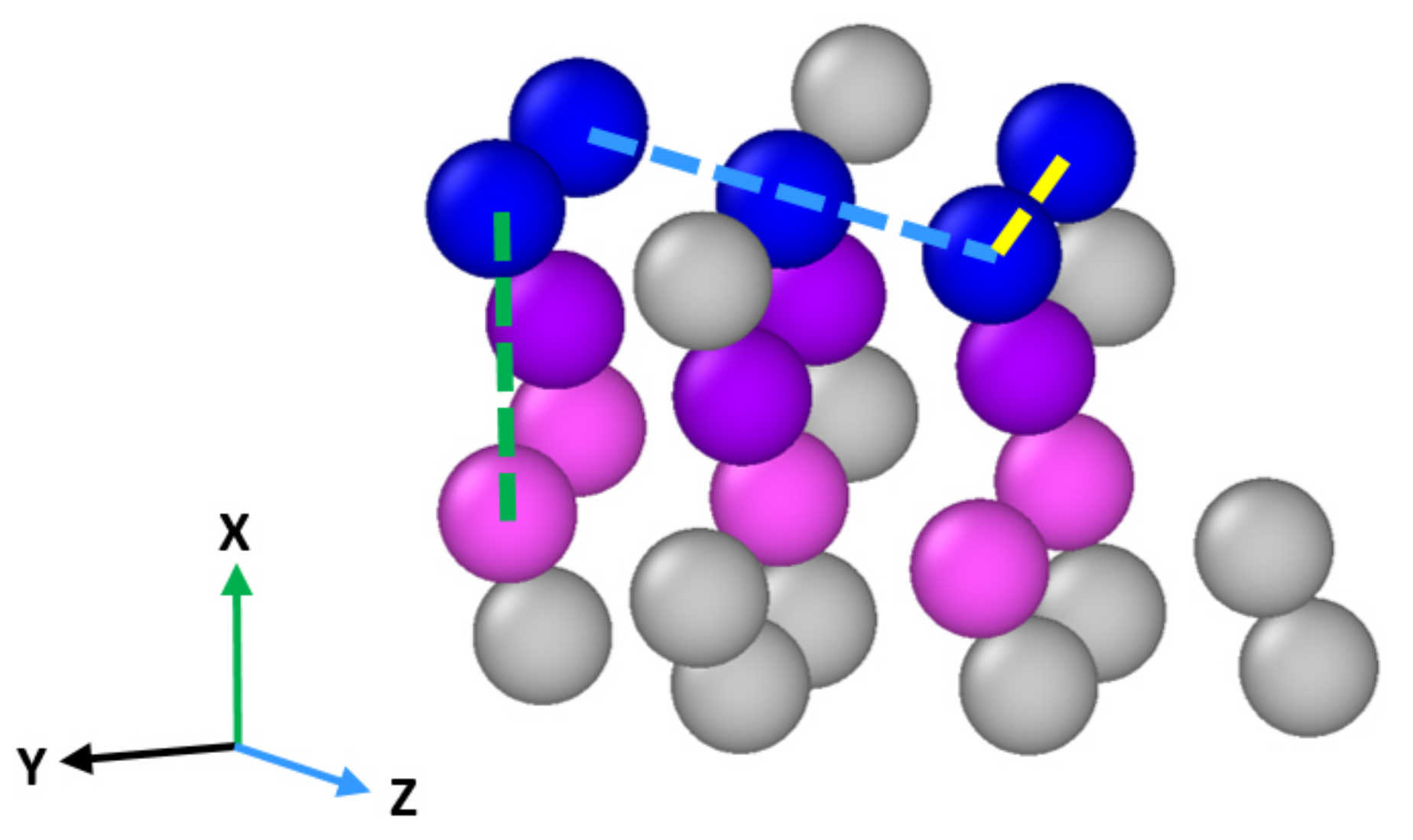
X
Y
Z

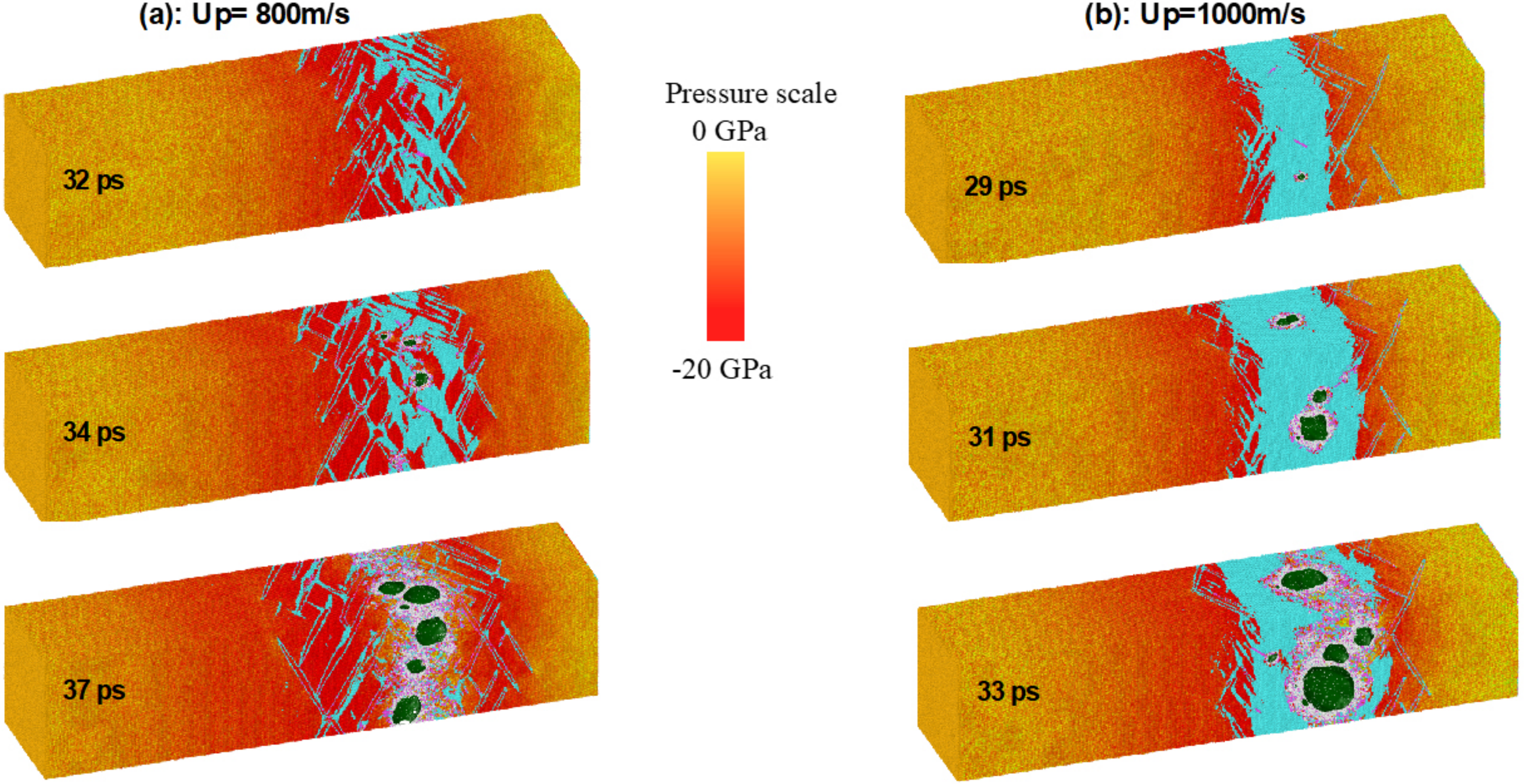
(a): Up= 800m/s
(b): Up=1000m/s
Pressure scale
0 GPa
-20 GPa
32 ps
34 ps
37 ps
29 ps
31 ps
33 ps

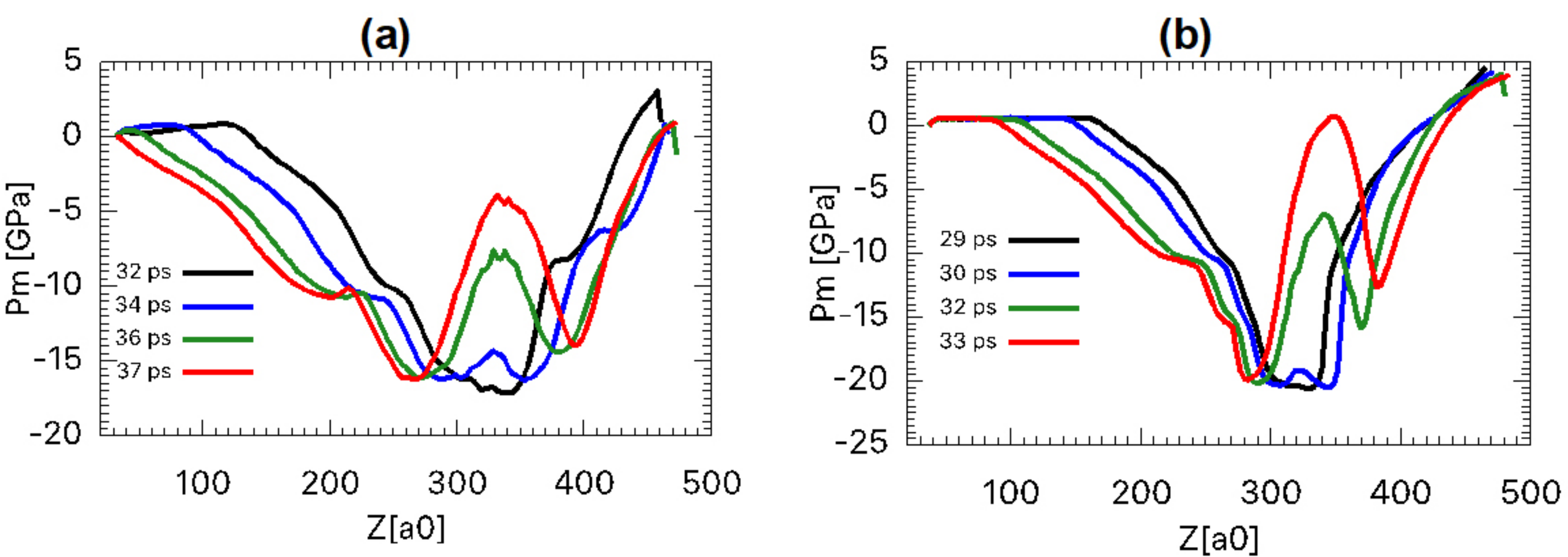
(a)
Pm [GPa]
Z[a0]
32 ps
34 ps
36 ps
37 ps
(b)
Pm [GPa]
Z[a0]
29 ps
30 ps
32 ps
33 ps

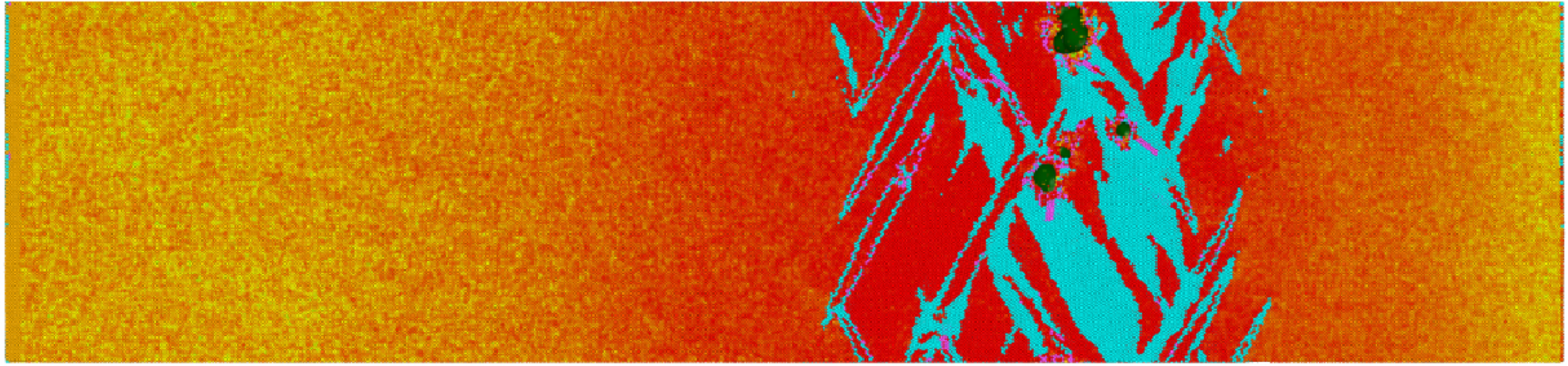

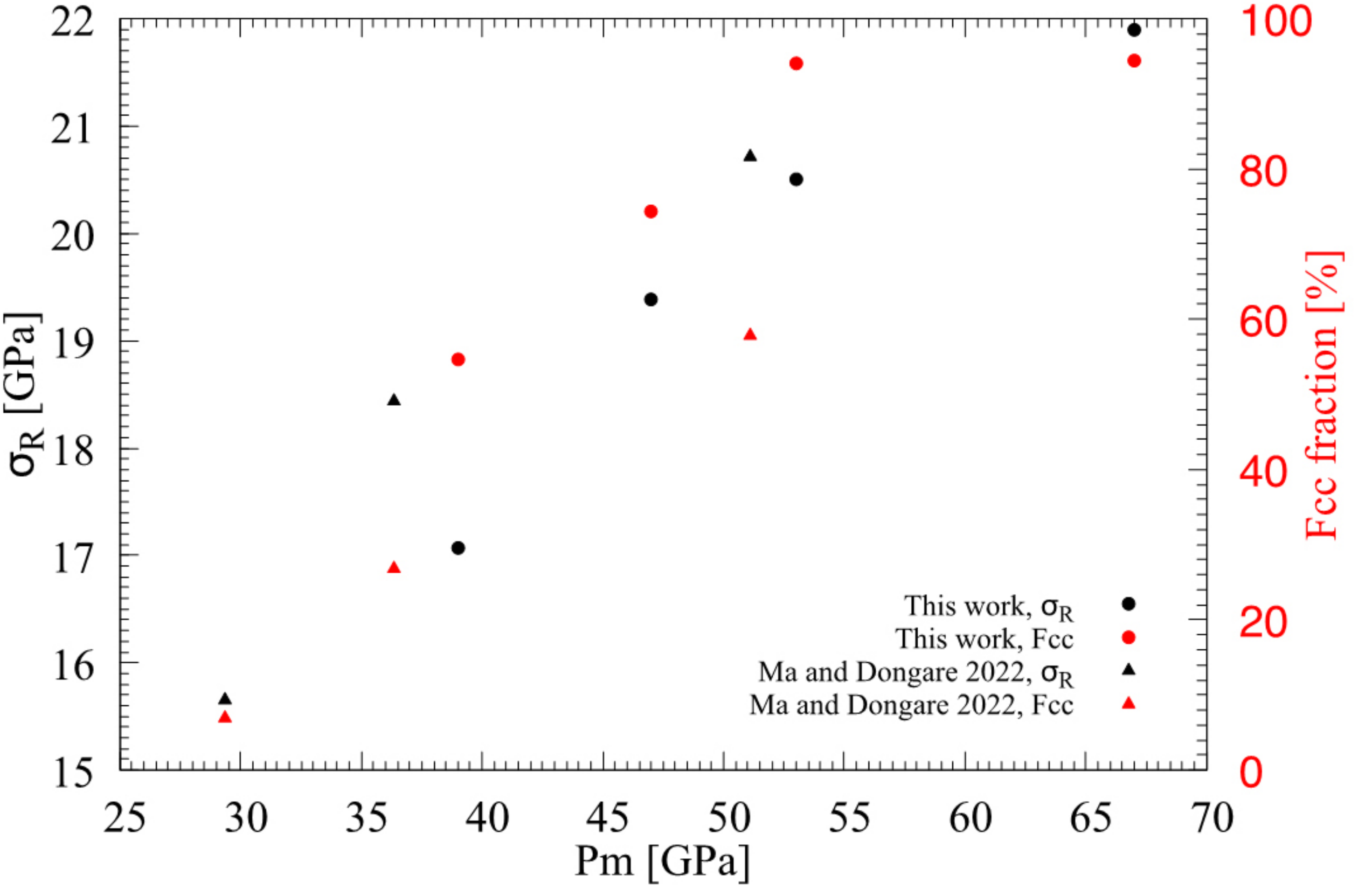
σR [GPa]
Fcc fraction [%]
Pm [GPa]
22
21
20
19
18
17
16
15
100
80
60
40
20
0
25
30
35
40
45
50
55
60
65
70
This work, σR
This work, Fcc
Ma and Dongare 2022, σR
Ma and Dongare 2022, Fcc

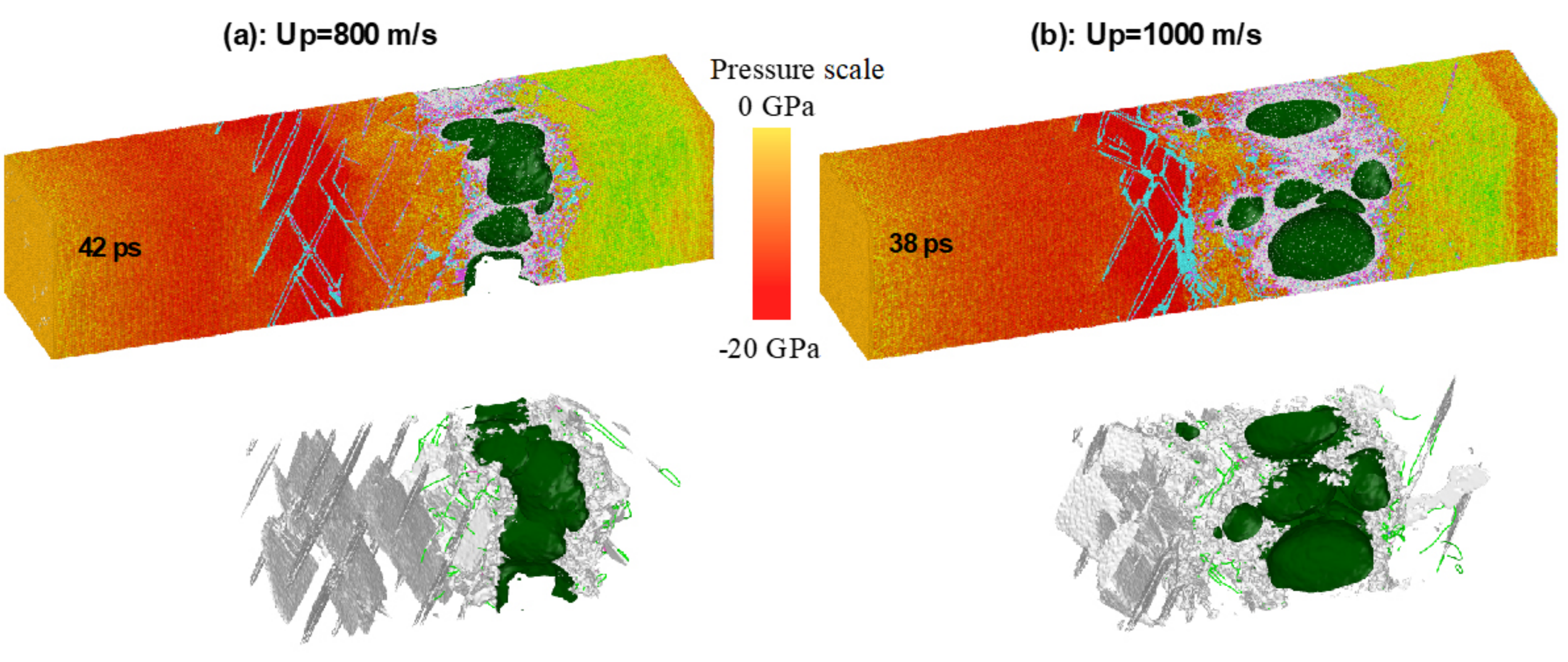
(a): Up=800 m/s
(b): Up=1000 m/s
Pressure scale
0 GPa
-20 GPa
42 ps
38 ps

(a):
Up = 800 m/s

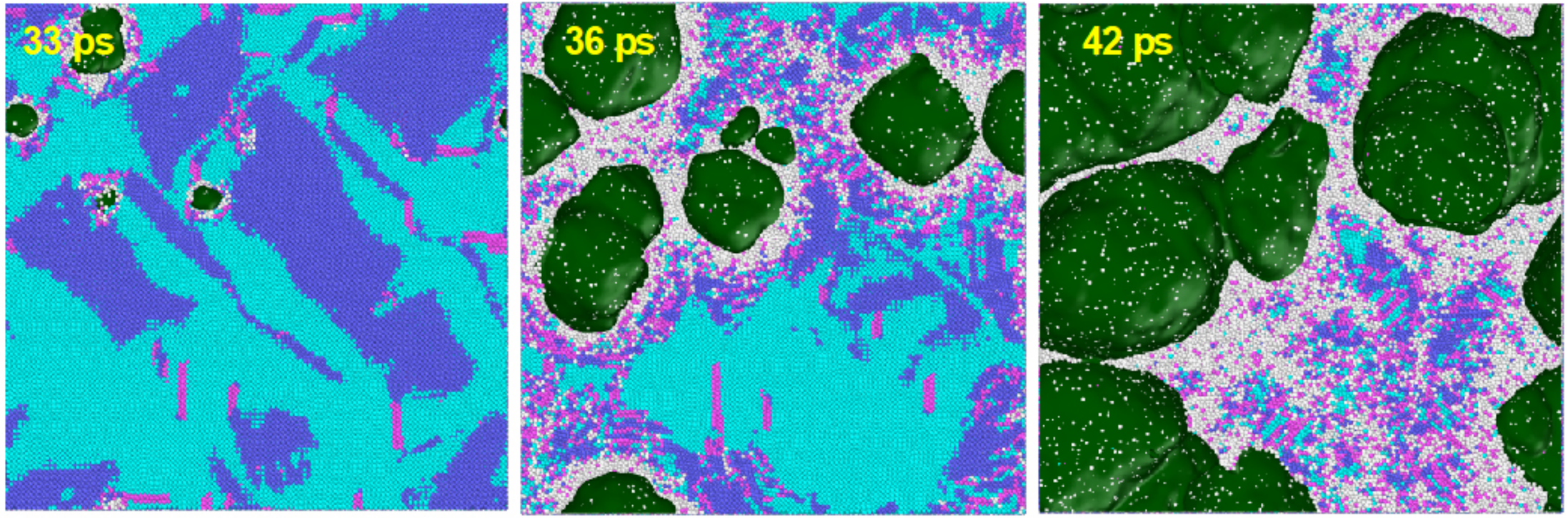

(b):
Up =1000m/s

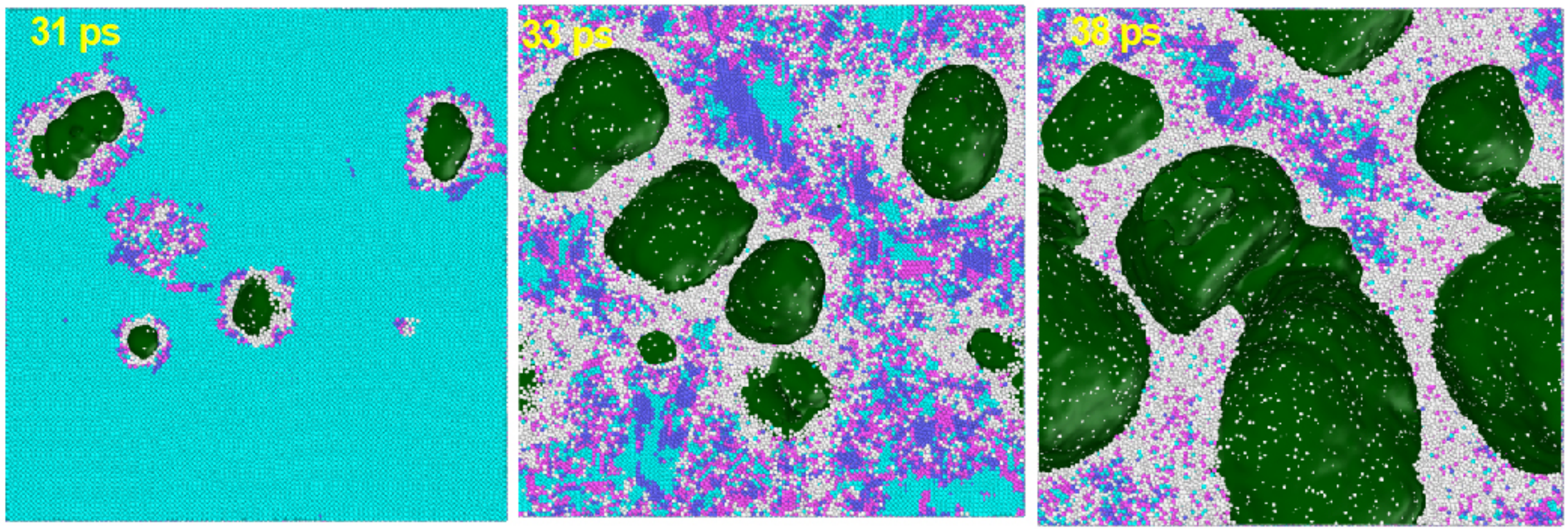

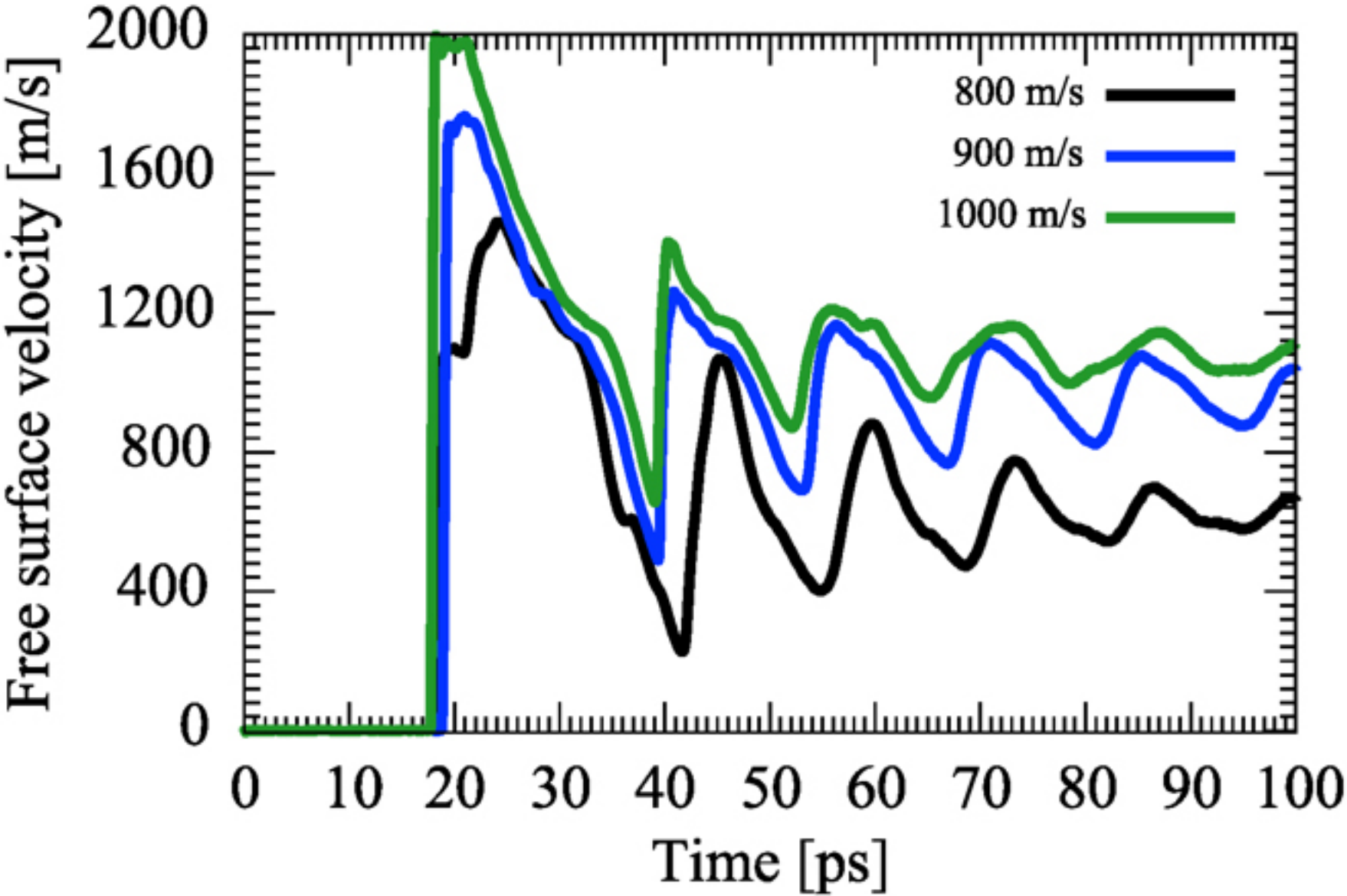
Free surface velocity [m/s]
2000
1600
1200
800
400
0
0
10
20
30
40
50
60
70
80
90
100
Time [ps]
800 m/s
900 m/s
1000 m/s